

Exposed water ice on the nucleus of comet 67P/Churyumov–Gerasimenko

G. Filacchione¹, M. C. De Sanctis¹, F. Capaccioni¹, A. Raponi¹, F. Tosi¹, M. Ciarniello¹, P. Cerroni¹, G. Piccioni¹, M. T. Capria¹, E. Palomba¹, G. Bellucci¹, S. Erard², D. Bockelee-Morvan², C. Leyrat², G. Arnold³, M. A. Barucci², M. Fulchignoni², B. Schmitt⁴, E. Quirico⁴, R. Jaumann³, K. Stephan³, A. Longobardo¹, V. Mennella⁵, A. Migliorini¹, E. Ammannito⁶, J. Benkhoff⁷, J. P. Bibring⁸, A. Blanco⁹, M. I. Blecka¹⁰, R. Carlson¹¹, U. Carsenty³, L. Colangeli⁷, M. Combes², M. Combi¹², J. Crovisier², P. Drossart², T. Encrenaz², C. Federico¹³, U. Fink¹⁴, S. Fonti⁹, W. H. Ip¹⁵, P. Irwin¹⁶, E. Kuehrt³, Y. Langevin⁸, G. Magni¹, T. McCord¹⁷, L. Moroz³, S. Mottola³, V. Orofino⁹, U. Schade¹⁸, F. Taylor¹⁶, D. Tiphene², G. P. Tozzi¹⁹, P. Beck⁴, N. Biver², L. Bonal⁴, J.-Ph. Combe¹⁷, D. Despan², E. Flaminii²⁰, M. Formisano¹, S. Fornasier², A. Frigeri¹, D. Grassi¹, M. S. Gudipati¹¹, D. Kappel³, F. Mancarella⁹, K. Markus³, F. Merlin², R. Orosei²¹, G. Rinaldi¹, M. Cartacci¹, A. Cicchetti¹, S. Giuppi¹, Y. Hello², F. Henry², S. Jacquinod², J. M. Reess², R. Noschese¹, R. Politi¹ & G. Peter²²

Although water vapour is the main species observed in the coma of comet 67P/Churyumov–Gerasimenko^{1,2} and water is the major constituent of cometary nuclei^{3,4}, limited evidence for exposed water-ice regions on the surface of the nucleus has been found so far^{5,6}. The absence of large regions of exposed water ice seems a common finding on the surfaces of many of the comets observed so far^{7–9}. The nucleus of 67P/Churyumov–Gerasimenko appears to be fairly uniformly coated with dark, dehydrated, refractory and organic-rich material¹⁰. Here we report the identification at infrared wavelengths of water ice on two debris falls in the Imhotep region of the nucleus. The ice has been exposed on the walls of elevated structures and at the base of the walls. A quantitative derivation of the abundance of ice in these regions indicates the presence of millimetre-sized pure water-ice grains, considerably larger than in all previous observations^{6,7–9}. Although micrometre-sized water-ice grains are the usual result of vapour recondensation in ice-free layers⁶, the occurrence of millimetre-sized grains of pure ice as observed in the Imhotep debris falls is best explained by grain growth by vapour diffusion in ice-rich layers, or by sintering. As a consequence of these processes, the nucleus can develop an extended and complex coating in which the outer dehydrated crust¹⁰ is superimposed on layers enriched in water ice. The stratigraphy observed on 67P/Churyumov–Gerasimenko^{11,12} is therefore the result of evolutionary processes affecting the uppermost metres of the nucleus and does not necessarily require a global layering to have occurred at the time of the comet's formation.

Located in the bottom part of the main lobe of 67P/Churyumov–Gerasimenko, the Imhotep plain is characterized by a smooth terrain unit 1 km × 1.5 km wide filled by very fine dust^{11,13}. The region is circumscribed by elevated structures, some of them showing a circular shape with well defined walls, which display erosion and mass wasting on their sides¹⁴. Rosetta's navigation cameras identified bright albedo patches (BAPs) on the walls of two of these features (Fig. 1): a flat-floored raised circular structure with an external rim partially collapsed located at the Ash–Khepry–Imhotep boundary at longitude 117° E, latitude 13° N (BAP1) and a hill with a steep slope at longitude 180°–182° E, latitude 4°–10° S (BAP2). Both areas are exposed towards the lower Imhotep plain where the waste material is accumulated as boulders and debris

at the bottom of the cliffs. These deposits are located on relatively cold, collapsed walls of elevated structures and seem to be recently exposed. The debris falls indicate material eroded and deposited at the base of walls. The overall geological context points to a process in which limited amounts of bedrock material break out of the wall and are distributed as disrupted fragments at the bottom of the affected wall regions. Mechanisms that can trigger the falls are related to water-ice sublimation, water-ice metamorphism, thermal cracking or possibly impacts.

The best views of the two BAPs obtained by the Visual InfraRed Thermal Imaging Spectrometer (VIRTIS-M)¹⁵ are shown in Fig. 2. The description of these observations, including the retrieval of the spectral parameters and the associated temperature maps, are discussed in the Methods.

In the two BAP regions, VIRTIS-M has detected prominent absorption features at 1.05 μm, 1.25 μm, 1.5 μm (partial), and 2.0 μm (discussed later in Fig. 3). These spectral features represent clear evidence of the presence of water ice. When observing the water-ice-rich areas, the 3.2-μm band, ubiquitously observed throughout the cometary nucleus and interpreted¹⁰ to be caused by the presence of organic compounds, appears to be deformed by the strong 3.0-μm signature of water ice. This is the case for the Hapi active region, where it appears in the form of transient deposits formed in the upper layer of the surface by recondensation of water molecules sublimated from sub-surface ice during the diurnal cycle⁶.

With the aim of verifying the spectral properties of the observed water-ice regions and to study their persistence during the first few months of the mission, we have performed a temporal analysis of the appearance of the 2-μm band while we use the entire 1–4-μm spectral range to derive the water-ice abundance and grain size quantitatively. In Fig. 3 we show the 2-μm band depth time series (see Methods for analysis details) for a BAP1 neighbourhood using all the spectra measured in the period 23 September to 21 November 2014 (Fig. 3a, b) and for BAP2 obtained between 2 and 23 September 2014 (Fig. 3c). The persistence of the 2-μm band absorption is evident during these time periods, resulting in average values of 5.6%–7.6% for BAP1 and 5.0% for BAP2.

The spectral analyses show not much change in the band centres and depths during the period of observation, indicating that the ice is

¹INAF-IAPS, Istituto di Astrofisica e Planetologia Spaziali, Rome, Italy. ²LESIA, Observatoire de Paris/CNRS/UPMC/Université Paris-Diderot, Meudon, France. ³Institute for Planetary Research, DLR, Berlin, Germany. ⁴Université Grenoble Alpes, CNRS, IPAG, Grenoble, France. ⁵INAF-Osservatorio di Capodimonte, Napoli, Italy. ⁶UCLA, Los Angeles, California, USA. ⁷European Space Agency—ESTEC, Noordwijk, The Netherlands. ⁸Institut d'Astrophysique Spatial CNRS, Orsay, France. ⁹Dipartimento di Matematica e Fisica "Ennio De Giorgi", Università del Salento, Lecce, Italy. ¹⁰Space Research Centre, Polish Academy of Sciences, Warsaw, Poland. ¹¹NASA JPL, Pasadena, California, USA. ¹²Space Physics Research Laboratory, The University of Michigan, Michigan, Ann Arbor, USA. ¹³Università di Perugia, Perugia, Italy. ¹⁴Lunar Planetary Laboratory, University of Arizona, Tucson, Arizona, USA. ¹⁵National Central University, Taipei, Taiwan. ¹⁶Department of Physics, Oxford University, Oxford, UK. ¹⁷Bear Fight Institute, Winthrop, Washington, USA. ¹⁸Helmholtz-Zentrum Berlin für Materialien und Energie, Berlin, Germany. ¹⁹INAF-Osservatorio Astrofisico di Arcetri, Firenze, Italy. ²⁰Agenzia Spaziale Italiana, Rome, Italy. ²¹Istituto di Radioastronomia—INAF, Bologna, Italy. ²²Institute of Optical Sensor Systems, DLR, Berlin, Germany.

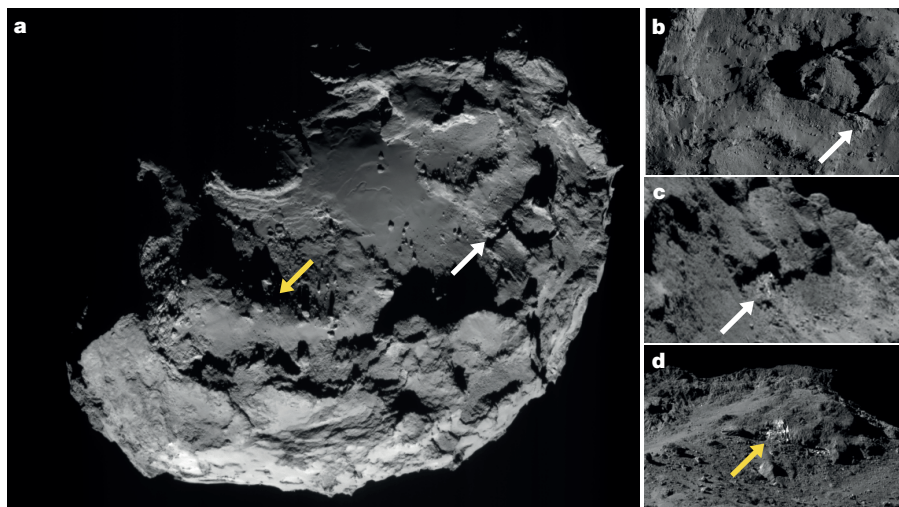


Figure 1 | Rosetta NAVCAM context images of the two debris falls. **a**, Imhotep region showing BAP1 on the Ash-Khepry-Imhotep boundary (white arrow) and BAP2 on the hillside (yellow arrow). **b**, Waste material and debris accumulated at the bottom of the landslide eroding the side of the elevated circular structure. BAP1 is not visible in the viewing geometry of this nadir-pointing image. **c**, BAP1 is caused by the presence of water ice, clearly visible on this oblique view of the elevated structure wall. **d**, Similar viewing geometry, identifying BAP2.

stable over that time frame. After linear spectral continuum removal, the $2.0\text{-}\mu\text{m}$ band centre appears to be located at $2.04\text{ }\mu\text{m}$ for BAP1 (Fig. 3d), with an average band depth of 5%. A band centre located at wavelengths slightly longer than $2.0\text{ }\mu\text{m}$ is diagnostic of crystalline water ice, as opposed to the amorphous ice phase, which has the band centre located at $2.0\text{ }\mu\text{m}$ (ref. 16). A secondary minimum of the $1.5\text{-}\mu\text{m}$ band, located at about $1.65\text{ }\mu\text{m}$, is a typical feature of water ice in the crystalline form (it is absent in amorphous ice¹⁷); in Fig. 3e, the VIRTIS-M data partially show the long-wavelength wing of the $1.5\text{-}\mu\text{m}$ band, in which the secondary minimum at about $1.65\text{ }\mu\text{m}$ is clearly seen. Finally, in a few well resolved pixels the weaker $1.05\text{-}\mu\text{m}$ and $1.25\text{-}\mu\text{m}$ bands of water ice have also been identified (Fig. 3e).

VIRTIS-M reflectance spectra were modelled following the approach described in the Methods. The best-fitting result shown in Fig. 4a, for a representative spectrum of BAP1, corresponds to an areal

mixing in which 1.2% of the pixel area is occupied by patches of large grains of diameter around 2 mm for this specific case of pure water ice while the remaining 98.8% of the pixel area is composed of an intimate mixture of water ice (3.4%, grains of diameter $56\text{ }\mu\text{m}$) and dark terrain (95.4%). As a result, the total amount of surface water ice on the simulated spectrum corresponds to about 4.6%, assuming each pixel samples an area of about $2.5\text{ m} \times 2.5\text{ m}$. By repeating this fitting technique on each pixel of the two high-resolution images shown in Fig. 2c–e, we have derived water-ice abundance maps for the two debris falls in which intimate and areal mixing of ice coexist within the dark terrain (Fig. 4b–e). The maximum water-ice abundances, equivalent to about 1.2% and 4% for the areal and intimate cases respectively, correspond to those of the bluish waste material accumulated at the base of the two debris falls. A similar water-ice abundance (6%) was observed by the Deep Impact mission on the 0.5-km^2 -wide water ice

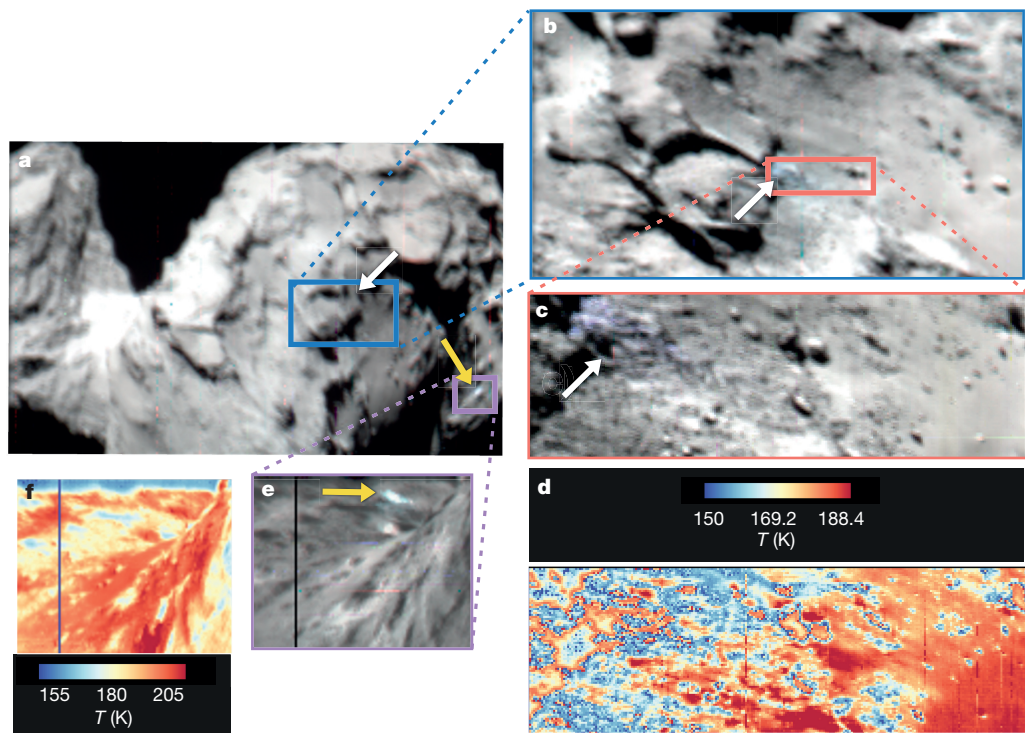


Figure 2 | VIRTIS-M observations of the two water-ice debris falls. **a**, Colour image showing BAP1 and BAP2 (white and yellow arrows, respectively). **b**, Water-ice-rich waste terrain on BAP1 is visible (blue) on the right side of the circular elevated structure. **c**, Close-up image acquisition of BAP1 reveals the bluish colour of the water-ice-rich unit.

d, Temperature map showing the water-ice-rich terrain at $T < 160\text{ K}$. **e**, Hillside image showing BAP2. **f**, Temperature map showing the water-ice-rich terrain at $T < 180\text{ K}$. **g**, Temperature map showing the water-ice-rich terrain at $T < 205\text{ K}$. All colour images are obtained from the $B = 1.3\text{ }\mu\text{m}$, $G = 2.0\text{ }\mu\text{m}$ and $R = 2.9\text{ }\mu\text{m}$ channels.

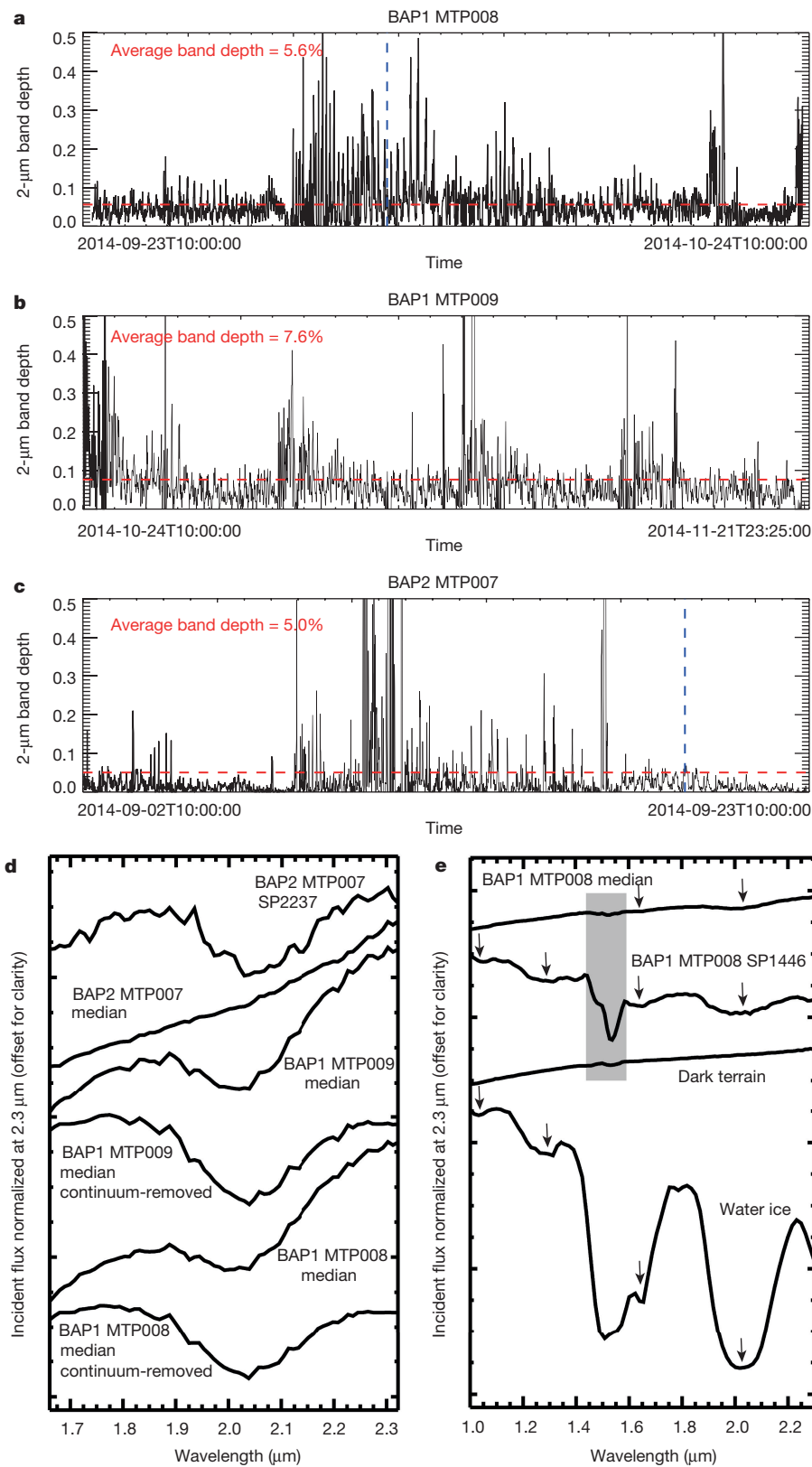


Figure 3 | Spectral evidence of water ice.

a, b, 2-μm band depth time series for BAP1 in October (MTP008) and November (MTP009) 2014. **c**, Same as panels **a** and **b** but for BAP2 in September (MTP007) 2014. Fluctuations are caused by the varying signal-to-noise ratio, owing to the changing illumination and viewing conditions during the observations. **d**, Median spectra derived from the MTP008 and MTP009 data sets for BAP1, showing the 2-μm absorption feature. Continuum-removed data show the spectral position of the band centre at about 2.04 μm, compatible with water ice in crystalline form. The 2-μm feature is not evident on the BAP2 median spectrum derived from the entire MTP007 data set; it appears only on limited observations, like the SP2237 one, marked by a blue vertical dashed line in **c**. SP2237 and SP1446 are the 2237th and 1446th spectra of the timeseries. **e**, The BAP1 median spectrum shows the 1.65-μm and 2-μm bands. A water-ice-rich pixel (SP1446, indicated by the blue dashed line in **a**) shows the 1.05-μm, 1.25-μm, 1.5–1.65-μm and 2.05-μm pure crystalline water-ice absorption features. This spectrum can be simulated with two endmembers, for example, crystalline water ice and dark terrain, as shown in Fig. 4. Instrumental order sorting filter junction wavelengths are marked by grey box.

deposits identified, by using a linear mixing technique, on the surface of comet 9P/Tempel 1 (ref. 7).

The size range of ice grains that produces the best fits in the observed areas displays a clear bimodal distribution (Extended Data Fig. 1), where 76% of the pixels in the intimate mixtures have grain sizes of 33–72 μm, and 68% of the pixels in the pure ice regions have grain sizes of 1.4–2.6 mm. Previously⁶, we showed that the diurnal mechanism of

ice trapping in the dehydrated uppermost layer led to the formation of ice grains only a few micrometres in diameter. Thus, the VIRTIS-M observations indicate the presence of three different populations of icy grains on the nucleus surface, which implies different growth mechanisms operating on different spatial scales and timescales.

Small water-ice grains are the result of the fast condensation process occurring for each comet rotation on the Hapi area in the thin

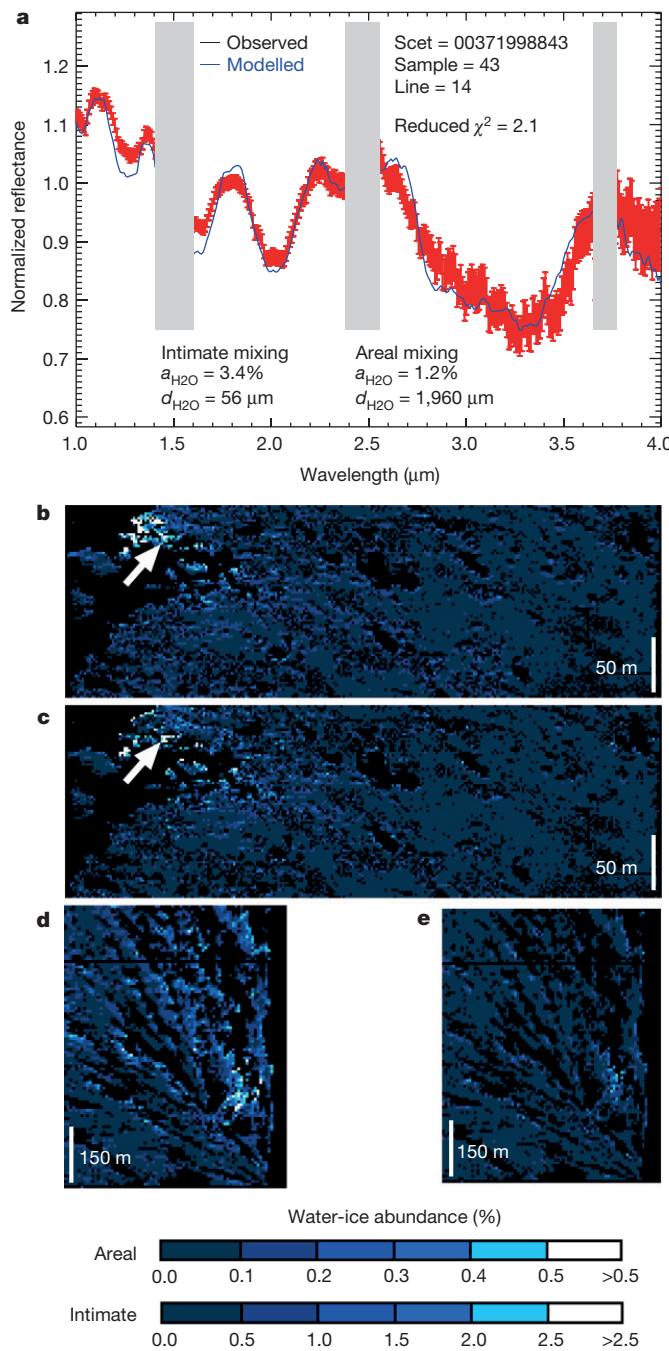


Figure 4 | Water-ice spectral analysis and spatial distribution. a, BAP1 water-ice-rich VIRTIS spectrum (black curve with error bars in red; at each wavelength the error corresponds to the inverse of the signal-to-noise ratio) and best-fit synthetic model (blue curve). $a_{\text{H}_2\text{O}}$ is the percentage of water ice and $d_{\text{H}_2\text{O}}$ is the water-ice grain size. ‘Scet’ is the spacecraft time used to identify the observation; ‘sample’ and ‘line’ correspond to the position of the pixel on the image. The location of the VIRTIS spectrum corresponds to the pixel indicated by an arrow in b and c. Instrumental order sorting filter junction wavelengths are marked by grey boxes. b, c, Water-ice abundance maps for BAP1 on observation I1_00371998843 (Fig. 2c) in areal (b) and intimate (c) mixing with dark material, respectively. d, e, Water-ice abundance maps for BAP2 on observation I1_00369369214 (Fig. 2e) in areal (d) and intimate (e) mixing with dark material, respectively. Black pixels in b–e correspond mainly to shadow areas whose spectra are excluded from the analysis because they have a median signal-to-noise ratio <30 , and for which a satisfactory model fit was not obtained. The estimated relative error for retrieved parameters is 20%.

(centimetre-sized) uppermost ice-free layers⁶. This is consistent with Deep Impact observations of the size distribution of ice grains released immediately after the impact event¹⁸. On the other hand, the occurrence of millimetre-sized grains of ‘pure’ (that is, water) ice, as observed over large areas (metre-sized) on the Imhotep debris falls, represents the occasional exposure of deeper layers which have been subjected to a more complex history. Assuming a size range of tens of micrometres as a typical size for ice grains present on the nucleus of comets (refs 7–9 and this work), the observations of millimetre-sized grains can be explained by the growth of secondary ice crystals from vapour diffusion in ice-rich colder layers and/or by ice grains sintering^{19,20}. The energy necessary to activate these processes is provided by the thermal heat wave penetrating into the subsurface layers and causing ice sublimation; the additional contribution to the total energy balance derived from the amorphous to crystalline phase transition should not be neglected, although it is expected to be moderate in size¹⁹. Ice grain growth can profoundly alter the thermal evolution of the nucleus because it causes a decrease in porosity (densification) and an increase in thermal conductivity. Models show that the ice grain growth and the densification can encompass layers of several metres²⁰, thus affecting the large-scale structural and thermal properties of the nucleus. Moreover, the KOSI experimental results showed that, depending on the dust-to-ice ratio, more than 80% of the sublimating ice was not released through the dust mantle but re-deposited at greater depths²¹. As a consequence, the observed stratification, which is one of the most prominent structural features of comet 67P/Churyumov–Gerasimenko^{11,12}, would be the result of cometary evolution processes rather than a remnant of the nucleus formation scenario.

Online Content Methods, along with any additional Extended Data display items and Source Data, are available in the online version of the paper; references unique to these sections appear only in the online paper.

Received 8 August; accepted 28 October 2015.

Published online 13 January 2016.

- Hässig, M. et al. Time variability and heterogeneity in the coma of 67P/Churyumov–Gerasimenko. *Science* **347**, <http://dx.doi.org/10.1126/science.aaa0276> (2015).
- Gulkis, S. et al. Subsurface properties and early activity of comet 67P/Churyumov–Gerasimenko. *Science* **347**, <http://dx.doi.org/10.1126/science.aaa0709> (2015).
- Mumma, M. J. & Charnley, S. B. The chemical composition of comets—emerging taxonomies and natal heritage. *Annu. Rev. Astron. Astrophys.* **49**, 471–524 (2011).
- Ehrenfreund, P., Charnley, S. B. & Wooden, D. H. in *Comets II* (eds Festou, M. C., Keller, H. U. & Weaver, H. A.) 115–133 (Univ. of Arizona Press, 2004).
- Pommerol, A. et al. OSIRIS observations of meter-size exposures of H_2O ice at the surface of 67P/Churyumov–Gerasimenko and interpretation using laboratory experiments. *Astron. Astrophys.* **583**, A25 (2015).
- De Sanctis, M. C. et al. The diurnal cycle of water ice on comet 67P/Churyumov–Gerasimenko. *Nature* **525**, 500–503 (2015).
- Capaccioni, F. et al. The organic-rich surface of comet 67P/Churyumov–Gerasimenko as seen by VIRTIS/Rosetta. *Science* **347**, <http://dx.doi.org/10.1126/science.aaa0628> (2015).
- Sunshine, J. M. et al. Exposed water ice deposits on the surface of comet 9P/Tempel 1. *Science* **311**, 1453–1455 (2006).
- A'Hearn, M. F. et al. EPOXI at comet Hartley 2. *Science* **332**, 1396–1400 (2011).
- Sunshine, J. M. et al. The distribution of water ice on comet 103P/Hartley 2. *Lunar Planet. Inst. Contrib.* **1667**, 6438 (2012).
- Thomas, N. et al. The morphological diversity of comet 67P/Churyumov–Gerasimenko. *Science* **347**, <http://dx.doi.org/10.1126/science.aaa0440> (2015).
- Massironi, M. et al. Two independent and primitive envelopes of the bilobate nucleus of comet 67P. *Nature* **526**, 402–405 (2015).
- Sierks, H. et al. On the nucleus structure and activity of comet 67P/Churyumov–Gerasimenko. *Science* **347**, <http://dx.doi.org/10.1126/science.aaa1044> (2015).
- Auger, A. T. et al. Geomorphology of the Imhotep region on comet 67P/Churyumov–Gerasimenko from OSIRIS observations. *Astron. Astrophys.* **583**, A35 (2015).
- Coradini, A. et al. Virtis: an imaging spectrometer for the Rosetta mission. *Space Sci. Rev.* **128**, 529–559 (2007).
- Grundy, W. M. & Schmitt, B. The temperature-dependent near-infrared absorption spectrum of hexagonal H_2O ice. *J. Geophys. Res.* **103**, 25809–25822 (1998).

17. Mastrapa, R. M. *et al.* Optical constants of amorphous and crystalline H₂O ice in the near infrared from 1.1 to 2.6 μm. *Icarus* **197**, 307–320 (2008).
18. Sunshine, J. M. *et al.* The distribution of water ice in the interior of comet Tempel 1. *Icarus* **190**, 284–294 (2007).
19. Prialnik, D., Benkhoff, J. & Podolack, M. in *Comets II* (eds Festou, M. C., Keller, H. U. & Weaver, H. A.) 115–133 (Univ. Arizona Press, 2004).
20. Kossacki, K. J., Szutowicz, S. L. & Leliwa-Kopystyński, J. Comet 46P/Wirtanen: evolution of the subsurface layer. *Icarus* **142**, 202–218 (1999).
21. Benkhoff, J., Seidensticker, K. J., Seiferlin, K. & Spohn, T. Energy analysis of porous water ice under space-simulated conditions: results from the KOSI-8 experiment. *Planet. Space Sci.* **43**, 353–361 (1995).

Acknowledgements We thank the following institutions and agencies, which supported this work: Italian Space Agency (ASI, Italy), Centre National d'Etudes Spatiales (CNES, France), Deutsches Zentrum für Luft- und Raumfahrt (DLR, Germany), National Aeronautic and Space Administration (NASA, USA). VIRTIS was built by a consortium from Italy, France and Germany, under the scientific responsibility of the Istituto di Astrofisica e Planetologia Spaziali (IAPS) of INAF, Rome (Italy), which also led the scientific operations. The VIRTIS instrument development for the ESA has been funded and managed by ASI, with contributions from Observatoire de Meudon financed by CNES and from the DLR. The VIRTIS instrument industrial prime contractor was

former Officine Galileo, now Selex ES (Finmeccanica Group) in Campi Bisenzio, Florence, Italy. We also thank the Rosetta Liaison Scientists, the Rosetta Science Ground Segment and the Rosetta Mission Operations Centre for their support in planning the VIRTIS observations. This research has made use of NASA's Astrophysics Data System. This work is dedicated to Angioletta Coradini, conceiver of the VIRTIS instrument.

Author Contributions G.F., M.C.D.S. and F.C. contributed to the data analysis and to the writing of the manuscript. G.F. and F.C. provided calibrated VIRTIS data. A.R. and M.C. provided the spectral fit. F.T. retrieved the temperatures. S.E., S.J., F.T. and C.L. provided geometry information. F.C., G.F., S.E., D.B.-M. and C.L. planned VIRTIS observations with R.N., M.C., A.C. and F.H. implementing telecommands sequences. R.P. and F.H. processed telemetry and data packets. All authors are instrument team members contributing to the discussion of the results.

Author Information The VIRTIS calibrated data will be available through the ESA's Planetary Science Archive (PSA) website by early 2016 (<http://www.rssd.esa.int>). Reprints and permissions information is available at www.nature.com/reprints. The authors declare no competing financial interests. Readers are welcome to comment on the online version of the paper. Correspondence and requests for materials should be addressed to G.F. (gianrico.filacchione@iaps.inaf.it).

METHODS

VIRTIS-M. VIRTIS-M is the visible–infrared hyperspectral channel¹⁵ aboard Rosetta. The instrument performs 0.25–5.1-μm spectroscopy by using two separate detectors: a charge-coupled device (CCD) for the 0.25–1-μm range and a HgCdTe for the 1.0–5.1-μm range, respectively. The spectral sampling is equal to 1.8 nm per band and 9.7 nm per band for the two channels, respectively. Both spectral channels share the same telescope equipped with a scanning mirror to build hyperspectral cubes. The instrumental field of view is equal to 3.7° with an instantaneous field of view of 250 μrad. The slit aperture is therefore acquired by 256 spatial samples. The raw data are converted to incident solar flux by applying the calibration pipeline^{22–24} and the corrections derived from in-flight data^{25,26}.

Observation campaigns. During the Philae pre-landing phase, four different nucleus mapping campaigns were carried out by VIRTIS-M: the first in August 2014, during the Medium Term Plan (MTP) mission period (MTP006), when the spacecraft was orbiting between distances of 50–100 km from the nucleus with solar phase angle 25°–40°. In this period many observations were made at constant solar phase (about 30°) with spatial resolution of 12.5–25 m per pixel, including the observation shown in Fig. 2a, in which both debris falls are shown. The second phase occurred in September 2014, during MTP007, when the spacecraft was at a distance of about 30 km with solar phase angle 60°–70°. During this campaign, both debris falls were observed by VIRTIS-M in oblique view with a spatial resolution of about 7.5 m per pixel (Fig. 2b, e). The third campaign (MTP008) was executed in October 2014 when the spacecraft orbited along the nucleus’ terminator in circular orbits at distances of 20 km and then 10 km, resulting in observations with a spatial resolution of 5–2.5 m per pixel taken at a solar phase angle of 90°. During the 10-km orbit VIRTIS-M acquired the best view of the waste material at the bottom of BAP1 (see Fig. 2c). Finally, the last campaign was executed from end of October to mid-November 2014 in preparation for the Philae lander release when the spacecraft’s trajectory was on a elliptic orbit at distances of between 10 km and 20 km, with VIRTIS-M continuing to monitor the nucleus with spatial resolution between 2.5 m and 5 m per pixel with solar phase angle between 70° to 100°. During this period the visibility of BAP1 continued to be good while BAP2 was no longer visible.

To take into account the local irregular topography we have expanded the range of coordinates over which our spectral analysis is performed to longitude 114°–120° E, latitude 11°–15° N for BAP1 and to longitude 178°–184° E, latitude 2°–12° S for BAP2. Overall, the best viewing of the two BAPs occurs during off-nadir pointing sequences and during Rosetta’s terminator orbits, when the emission angle on the exposed walls is smaller. The analysis of VIRTIS geo-referenced images of these areas shows that a total of 7,495 and 7,204 VIRTIS pixels in day-side illumination conditions are located above BAP1 and BAP2, respectively. The corresponding 2-μm water-ice band depth above these points is shown in Fig. 3a–c for the different MTP intervals. Fluctuations are due to the variable water-ice distribution above the local rough topography with different illumination and viewing geometry occurring during Rosetta’s orbits around the comet.

Thermal images. For the two better resolved observations of the debris fall regions, thermal images are shown in Fig. 2d–f at the same scale as the corresponding images in reflectance. VIRTIS-M data are used to derive the surface temperature by modelling spectral radiance in the 4.5–5.1-μm range, adopting a Bayesian approach²⁷. The retrieved temperature of a given point on the surface of the nucleus is a function of the local terrain properties (albedo, composition, grain size, roughness, thermal conductivity, volatiles sublimation) and illumination geometry (solar incidence angle, local solar time, time since last shadow occurred). As a consequence of the large obliquity of the spin axis with respect to the orbital plane, the southern hemisphere, where the Imhotep plain is located, is considerably less illuminated than the northern hemisphere until a few months before perihelion passage (which occurred in August 2015). This affects the average temperatures measured on this region, which are much lower than the ones measured on the smaller nucleus lobe and in the north part of the larger one^{2,28}. On the Imhotep plain, the MIRO experiment has measured a maximum diurnal subsurface temperature of about 120 K with both millimetre and submillimetre channels² while modelling VIRTIS-M data a diurnal surface temperature of 180–190 ± 15 K has been inferred²⁸. Such thermal conditions are favourable for preserving water ice on the surface²⁹. In addition, Fig. 2d–f clearly shows that BAP1 and BAP2 are on average cooler than nearby terrains. In the thermal image of BAP1, VIRTIS-M has measured a temperature lower than 160 ± 30 K on pixels where water-ice features are more prominent. On BAP2, the temperature is below 180 ± 15 K. This means that in both regions the water ice is close to the sublimation regime²⁹.

Spectral modelling. A quantitative spectral analysis of the composition of BAP1 and BAP2 has been performed using Hapke’s radiative transfer model³⁰ as described in ref. 31. The two regions have been modelled using a complex mixture of two spectral endmembers: crystalline water ice, simulated by using optical constants^{17,32–34} measured at $T = 160$ K between 1 μm and 4 μm, and a ‘dark terrain’

unit corresponding to the average spectrum of the comet’s surface after the application of photometric correction³⁵. Both endmember spectra are shown in Fig. 3e in the 1.0–2.3 μm spectral range. The analysis has been performed on spectra normalized at 2.3 μm in order to rule out uncertainties on the radiometric and photometric accuracy as well as errors on the local geometry information, owing to unresolved shadows and roughness.

According to Hapke’s theory³⁰ the ratio of the bidirectional reflectance $r(i, e, g, \lambda)$ of a semi-infinite medium taken at two wavelengths λ and λ_0 can be expressed as $r(i, e, g, \lambda)/r(i, e, g, \lambda_0)$, where:

$$r(i, e, g, \lambda) = \frac{w(\lambda)K}{4\pi} \frac{\mu_{0e}}{\mu_{0e} + \mu_e} [B_{SH}(g)p(g, \lambda)] \\ + [H(w(\lambda), \mu_{0e} / K)H(w(\lambda), \mu_e / K) - 1]S(i, e, g, \theta)B_{CB}(g, \lambda) \quad (1)$$

and

$$r(i, e, g, \lambda_0) = \frac{w(\lambda_0)K}{4\pi} \frac{\mu_{0e}}{\mu_{0e} + \mu_e} [B_{SH}(g)p(g, \lambda_0)] \\ + [H(w(\lambda_0), \mu_{0e} / K)H(w(\lambda_0), \mu_e / K) - 1]S(i, e, g, \theta)B_{CB}(g, \lambda_0) \quad (2)$$

Here i , e and g are the incidence, emission and phase angle, respectively; w is the single scattering albedo; K is the porosity of the medium; $p(g, \lambda)$ is the single particle phase function; μ_{0e} and μ_e are the effective cosines of the incidence and emission angles, differing from μ_0 and μ because of the effect of surface roughness; $H(w, \mu_e / K)$ is the Chandrasekhar function describing the multiple scattering components; $B_{SH}(g)$ is the shadow hiding opposition effect term; $B_{CB}(g, \lambda)$ the coherent back-scattering opposition effect; $S(i, e, g, \theta)$ is the shadow function modelling large-scale roughness and θ is the average surface slope.

Taking the ratio $r(i, e, g, \lambda)/r(i, e, g, \lambda_0)$, all the terms that do not depend on wavelength will cancel each other out. In particular, the porosity K and the roughness embedded in the $S(i, e, g, \theta)$ shadow function are removed. Moreover, during the VIRTIS-M observations described in this paper the solar phase was fixed at $g = 95^\circ$. As a consequence the shadow hiding effect is negligible and this implies that the terms B_{SH} and B_{CB} are equal to 1.

In summary, the ratio $r(i, e, g, \lambda)/r(i, e, g, \lambda_0)$ will be simplified as follows:

$$\frac{r(i, e, g, \lambda)}{r(i, e, g, \lambda_0)} = \frac{w(\lambda)}{w(\lambda_0)} \left[\frac{p(g, \lambda) + H(w(\lambda), \mu_{0e} / K)H(w(\lambda), \mu_e / K) - 1}{p(g, \lambda_0) + H(w(\lambda_0), \mu_{0e} / K)H(w(\lambda_0), \mu_e / K) - 1} \right] \quad (3)$$

In addition, for the dark terrain component, which makes up the majority by far of the material present on the nucleus surface, the contribution of the porosity and of the roughness to the multiple scattering term is a second-order effect. Thus we can assume $\mu_{0e}/K = \mu_0$.

Equation (2) represents the formulation to be used to derive the normalized reflectance of a single material but it can be straightforwardly extended to the case of a linear combination of reflectances, maintaining the simplifications described above. In this relation the parameters to fit are the phase function $p(g)$ and the single scattering albedo w , which can be modelled using the optical constants and the grain size. The phase function $p(g)$ derived by ref. 35 is used in the spectral modelling.

We are dealing with two endmembers and we have used areal and intimate mixing modalities in the simulations: in the areal mixing the surface is modelled as patches of pure water ice and dark terrain, with each photon scattered within one patch. In the intimate mixing model the particles of the two endmember materials are in contact with each other and both are involved in the scattering of a single photon. In intimate mixing the single scattering albedo of the mixture is the weighted average, through their abundance P , of the dark terrain and water-ice single scattering albedos. Thus the $w(\lambda)$ is given by $w(\lambda) = w(\lambda)_{DT}P_{DT} + w(\lambda)_{WI}P_{WI}$. However, in the areal mixing (linear mixing), the two components are treated independently. For the dark terrain we have used the $w(\lambda)$ value retrieved from the photometric correction³⁵, while to describe the water ice contribution we explicitly calculated the $w(\lambda)$ from the optical constants and from the grain size, which represent the parameter to be fitted. Furthermore, after extensive tests, we have been able to fix the value of the phase function $p(g = 95^\circ) = 0.5$. With the approach described above, the model’s free parameters are the percentage and grain size of the water ice in the intimate mixed phase, and the percentage and grain size of the water ice in the areal mixed phase.

Before fitting, the observed spectra are corrected for spikes and for instrumental artefacts. The best-fitting result, an example of which is shown in Fig. 4a, is obtained by applying the Levenberg–Marquardt method for nonlinear least-squares multiple regression. In this specific case, the best matching spectrum corresponds to an areal mixing where $a_{H2O} = 1.2\%$ of the pixel area is modelled with large grains (size distribution peaked around $d_{H2O} = 2$ mm in diameter) of pure

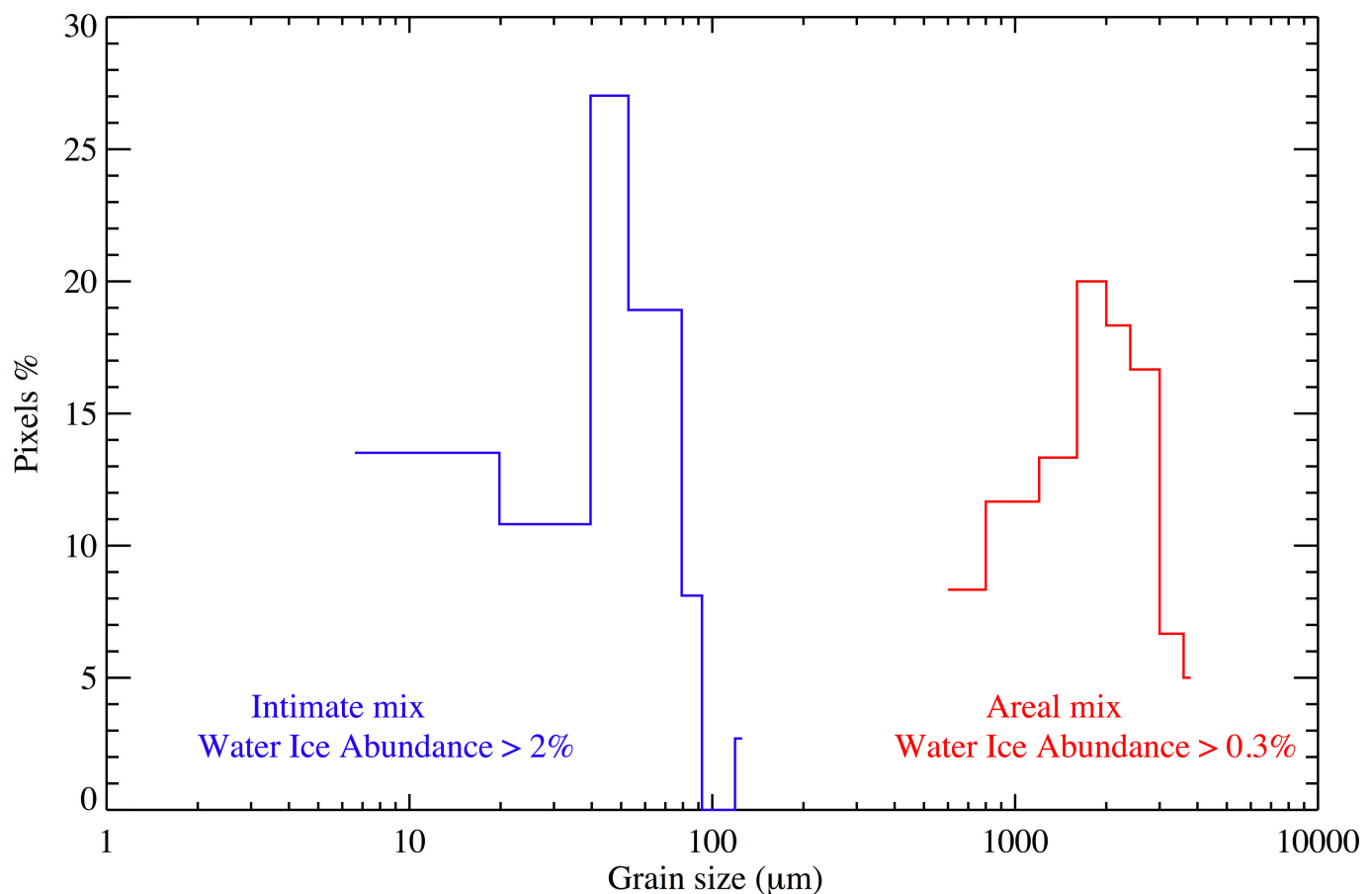
water ice while the remaining 98.8% of the pixel area is composed of an intimate mixture with $a_{\text{H}_2\text{O}} = 3.4\%$ of water ice (size distribution peaked at $d_{\text{H}_2\text{O}} = 56\text{ }\mu\text{m}$ in diameter) and the remaining 95.4% of dark material. The distribution of the areal and intimate grain sizes appears to be monodispersed (Extended Data Fig. 1) and grouped into two very different families: small grains of 50–60 μm diameter size in the intimate case and large millimetre-size grains in the areal case. When we say that our fit requires particles of average sizes of 2 mm, this means that, from a photon point of view, the medium is essentially continuous at scales of 2 mm. This implies that any discontinuities (for example, voids) within a volume of 2 mm radius should be smaller than the wavelength.

NAVCAM images references. The Rosetta NAVCAM context images of the two debris fall shown in Fig. 1 are: ROS_CAM1_20140823T184003, taken on 2014-08-23T18:40 (corresponding to 23 August 2014 at 18:40 Universal Standard Time) from a distance of 64.8 km (Fig. 1a). BAP1 on the Ash–Khepry–Imhotep boundary (at longitude 117° E, latitude 13° N) is indicated by the white arrow. BAP2 on the hillside (at longitude 180°–182° E, latitude 4°–10° S) is indicated by the yellow arrow; ROS_CAM1_20140914T121933, taken on 2014-09-14T12:19 from a distance of 30.7 km (Fig. 1b). The image shows the waste material and debris accumulated at the bottom of the landslide eroding the side of the elevated circular structure. BAP1 is not visible in the viewing geometry of this nadir-pointing image; ROS_CAM1_20140920T060854, taken on 2014-09-20T06:08 from a distance of 28.2 km (Fig. 1c). BAP1 is caused by the presence of water ice, clearly visible on the oblique view of the elevated structure wall; ROS_CAM1_20140915T021834, taken on 2014-09-15T02:18 from a distance of 29.9 km (Fig. 1d). This image shows a viewing geometry identifying BAP2 similar to Fig. 1c. Note a secondary smaller bright layer on the right of the primary.

VIRTIS-M hyperspectral cube references. The Rosetta VIRTIS-M observations of the two BAPs shown in Fig. 2 are as follows: I1_00367585390, taken on 2014-08-25T11:04 with an integration time of 3 s per line and a spatial resolution of 12.5 m per pixel (Fig. 2a); I1_00369364114, taken on 2014-09-15T01:09 with an integration time of 3 s per line and a spatial resolution of 7.5 m per pixel (Fig. 2b); I1_00371998843, taken on 2014-10-15T13:01 with an integration time of 3 s per line and a spatial resolution of 2.5 m per pixel (Fig. 2c, d); I1_00369369214, taken

on 2014-09-15T02:34 with an integration time of 3 s per line and a spatial resolution of 7.5 m per pixel (Fig. 2e, f).

22. Filacchione, G. Calibrazioni a terra e prestazioni in volo di spettrometri ad immagine nel visibile e nel vicino infrarosso per l'esplorazione planetaria. PhD dissertation, Univ. Studi di Napoli Federico II (2006); available at http://www.fedoa.unina.it/1462/1/Filacchione_Ingegneria_Aerospaziale_Navale_e_della_Qualita.pdf.
23. Ammannito, E. et al. On-ground characterization of Rosetta/VIRTIS-M. I. Spectral and geometrical calibrations. *Rev. Sci. Instrum.* **77**, 093109 (2006).
24. Filacchione, G. et al. On-ground characterization of Rosetta/VIRTIS-M. II. Spatial and radiometric calibrations. *Rev. Sci. Instrum.* **77**, 103106 (2006).
25. Migliorini, A. et al. Comparative analysis of airglow emissions in terrestrial planets, observed with VIRTIS-M instruments on board Rosetta and Venus Express. *Icarus* **226**, 1115–1127 (2013).
26. Raponi, A. Spectrophotometric analysis of cometary nuclei from in situ observations. PhD thesis, Univ. degli studi di Roma Tor Vergata (2014); preprint at <http://arxiv.org/abs/1503.08172>.
27. Tosi, F. et al. Thermal measurements of dark and bright surface features on Vesta as derived from Dawn/VIR. *Icarus* **240**, 36–57 (2014).
28. Tosi, F. et al. Thermal maps and properties of comet 67P as derived from Rosetta/VIRTIS data. *Lunar Planet. Sci. Conf.* **XXXVI**, 2156 (LPI contribution no. 1832, 2015).
29. Fray, N. & Schmitt, B. Sublimation of ices of astrophysical interest: a bibliographic review. *Planet. Space Sci.* **57**, 2053–2080 (2009).
30. Hapke, B. *Theory of Reflectance and Emittance Spectroscopy* (Cambridge Univ. Press, 2012).
31. Ciarniello, M. et al. Hapke modeling of Rhea surface properties through Cassini-VIMS spectra. *Icarus* **214**, 541–555 (2011).
32. Ciarniello, M. et al. Photometric properties of comet 67P/Churyumov–Gerasimenko from VIRTIS-M onboard Rosetta. *Astron. Astrophys.* **583**, A31 (2015).
33. Warren, S. G. Optical constants of ice from the ultraviolet to the microwave. *Appl. Opt.* **23**, 1206 (1984).
34. Mastrapa, R. M. et al. Optical constants of amorphous and crystalline H_2O -ice: 2.5–22 μm ($4000\text{--}455\text{ cm}^{-1}$) optical constants of H_2O -ice. *Astrophys. J.* **701**, 1347–1356 (2009).
35. Clark, R. N. et al. The surface composition of Iapetus: mapping results from Cassini VIMS. *Icarus* **218**, 831–860 (2012).



Extended Data Figure 1 | Water-ice grain size distribution derived from BAP1. Grains are present in two monodispersed distributions with maxima at 56 μm and at 2 mm, corresponding to the intimate and areal

mixing classes, respectively. The histogram is computed by selecting only pixels showing a water-ice abundance greater than 2% for the intimate mixing class and greater than 0.3% for areal mixing.